Journal of
Synchrotron
Radiation

ISSN 0909-0495

Received 11 September 2012
Accepted 16 January 2013

Quantitative visualization of a gas diffusion layer in a polymer electrolyte fuel cell using synchrotron X-ray imaging techniques

Seung Gon Kim and Sang Joon Lee*

Center for Biofluid and Biomimic Research, Department of Mechanical Engineering, Pohang University of Science and Technology, San 31, Hyoja Dong, Namgu, Pohang 790-784, Republic of Korea. E-mail: sjlee@postech.ac.kr

A gas diffusion layer (GDL) in a polymer electrolyte fuel cell (PEFC) is quantitatively visualized using synchrotron X-ray micro-computed tomography. For three-dimensional reconstruction, an adaptive threshold method is used. This method is compared with the conventional method, *i.e.* Otsu's method. Additionally, the spatial and temporal variations of the porosity distribution of the GDL under freeze-and-thaw cycles are investigated experimentally. The freeze-and-thaw cycles are established simply using a CRYO system and light source illumination, respectively. Structural defects are found to largely affect the porosity of the GDL. In addition, a cyclic porosity variation is observed in the GDL under freeze-and-thaw cycles. The heterogeneous porosity is irreversibly decreased with the progress of repetitive cycles.

Keywords: polymer electrolyte fuel cell; gas diffusion layer; porosity distribution; freeze-and-thaw cycle; X-ray tomography.

1. Introduction

A polymer electrolyte fuel cell (PEFC) consists of a Nafion polymer membrane, electrode catalysts, gas diffusion layers (GDLs) and bipolar plates. The Nafion membrane is commonly employed to transport ions from anode to cathode electrolyte. The ion conductivity of Nafion is closely related to the membrane hydration. The GDL, also known as the porous transport layer (PTL), is a porous medium through which reactant gases pass to the catalyst and discharge water to gas channels (Barbir, 2005). The PEFC system is usually employed in mobile applications owing to its relatively low operating temperature and proper power range for automobiles. However, it inevitably faces sub-zero conditions after shut down in winter. The freezing and thawing environment decreases the performance and durability of the PEFC (Cho *et al.*, 2003). The degradation of the cell performance is closely attributed to structural transformation of the Nafion membrane and GDL (Park *et al.*, 2010). A GDL is usually composed of carbon fibers or felts with binder materials and hydrophobic coating. Since the carbon fibers and felts are a few micrometers in diameter, the pores of the GDL have sizes of tens of micrometers. Owing to the random orientation of the fibers and felts, the GDL has an anisotropic structure. Therefore, the structural characteristics of the GDL, such as porosity, pore size and pore configuration, are key parameters for understanding the water transport in a PEFC system.

There are several methods of measuring the porosity of porous media. The most common method is mercury intrusion porosimetry (Gallagher *et al.*, 2008). The CRYO-SEM method has also been employed to visualize ice formation in a catalyst layer during freeze-and-thaw cycles (Li *et al.*, 2008). However, since the CRYO-SEM method is an invasive technique, it is not suitable for consecutive measurements. Recently, X-ray micro-computed tomography (μCT) was introduced to visualize the three-dimensional morphological structure of GDLs with high spatial resolution (Kim & Lee, 2012). Radon (1917) established the mathematical basis of the tomographic imaging method. In recent years, X-ray tomography has been adopted to investigate the internal structure of materials (Stock, 2008), and it was found to be adequate for *in situ* experiments (Deville *et al.*, 2009; Buffiere *et al.*, 2010). The X-ray imaging technique was employed to visualize water distribution in a PEFC (Lee, Kim, Park & Kim, 2010). By employing the X-ray μCT technique, the porosity distribution of a GDL in the through-plane direction was quantitatively analyzed (Fishman *et al.*, 2010).

In the present study, the three-dimensional structure of a GDL is quantitatively visualized using the μCT technique. In addition, by comparing the heterogeneous porosity distributions of the GDL in the freeze-and-thaw states, the regions of structural transformation are quantitatively estimated. Moreover, based on the model established for randomly oriented fibrous porous media (Tomadakis & Sotirchos, 1991), the

Table 1
Specifications of the Pohang Light Source beamline 7B2.

Light intensity	2.8 keV at 2 GeV; 5.5 keV at 2.5 GeV
Photon flux	$\sim 10^{13}$ photons s^{-1}
CCD pixels	1600 × 1200
Pixel size	0.36 × 0.36 μm
Field of view	580 × 435 μm
Spatial resolution	1 μm
Scintillator	$CdWO_4$ single crystal (150 μm)

variations of heterogeneous tortuosity and permeability are demonstrated in detail.

2. Experimental method and apparatus

2.1. Synchrotron X-ray μCT

Fig. 1 shows how to reconstruct a three-dimensional tomographic image of a sample. First, a large number of two-dimensional cross-sectional images are obtained consecutively by rotating the sample with a small angle of 0.5° over 180°. Ortho-sliced images are obtained from the cross-sectional images *via* arithmetic calculations using *OCTOPUS* (http://www.xraylab.com). Then, vertically sliced images are derived using coordinate transformation. From the coordinate transformation, 1336 images of 600 × 1300 pixels are converted to 600 images of 1336 × 1300 pixels for each experimental condition. All three-dimensional images handled in this study are reconstructed using *AMIRA* software (http://www.amira.com).

2.2. Experimental set-up

The present experiments were performed at the 7B2 beamline of the Pohang Accelerator Laboratory (PAL) (Pohang, Korea). The incident white beam has a photon energy of 2.8–5.5 keV and 10^{13} photon flux (photons s^{-1}). A charged-coupled device (CCD) camera having 1600 × 1200 pixels and 0.36 × 0.36 μm pixel size is used to capture two-dimensional X-ray images. The field of view is 580 × 435 μm in physical dimensions. The synchrotron X-ray imaging system has about 1 μm spatial resolution and specifications of the 7B2 beamline are summarized in Table 1.

Fig. 2 shows schematic diagrams of the experimental set-up of the synchrotron X-ray imaging system and the freezing and thawing devices around a rotational stage. All the X-ray experiments are performed in a well air-conditioned hutch. The temperature of the GDL sample is controlled by adjusting the distance between the sample and the jet nozzle of the liquid-nitrogen CRYO system or the thawing light source. The temperature for the freezing and thawing cycles is maintained at 243 K and 308 K, respectively. Each freezing and thawing cycle has a period of 5 min to achieve sufficient heat conduction. The GDL samples tested in this study were manufactured by SGL Carbon Group (USA). The model numbers of the carbon paper-type and the felt-type GDLs are 35BA and 10BA, respectively. Each GDL sample is stripped to 1 mm × 5 mm in physical dimensions. The experimental conditions employed in this study are summarized in Table 2.

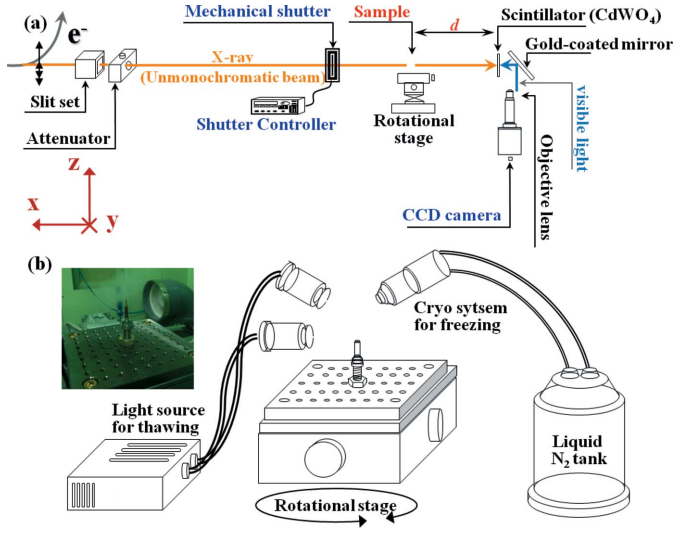

Figure 2
Experimental set-up for X-ray μCT. (*a*) Schematic diagram of the synchrotron X-ray imaging system. (*b*) Freeze-and-thaw devices around a rotational stage.

3. Results and discussion

3.1. Image segmentation

In the image segmentation, proper thresholding is essential for distinguishing solid regions from void regions. Finding an

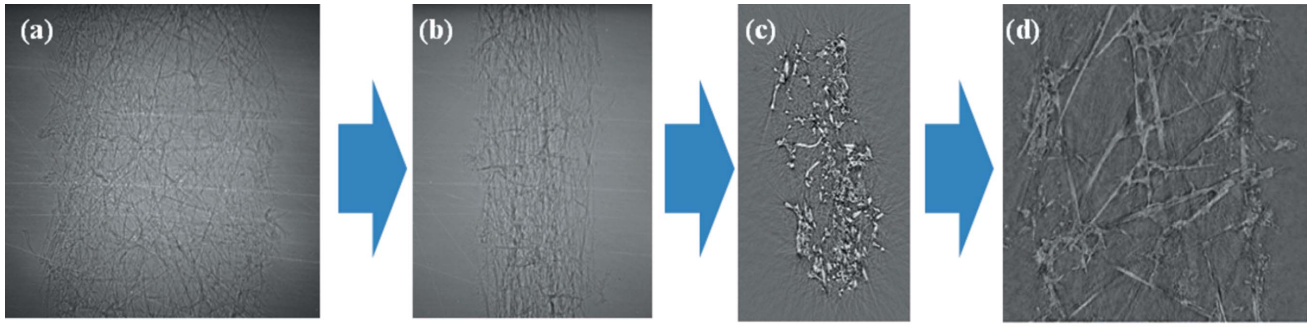

Figure 1
Procedure of the three-dimensional tomographic image reconstruction using X-ray μCT.

Table 2
Experimental conditions of the freeze-and-thaw state.

Hutch temperature	300 K
Hutch relative humidity	57%
Freezing temperature	243 K
Thawing temperature	308 K
Freeze-and-thaw cycle period	5 min/5 min
Sample size	1 mm × 5 mm

optimal threshold value is crucial to enhance the accuracy of the computed-tomography measurement. Recently, Otsu's thresholding method (Otsu, 1979) has been widely employed for image segmentation. The method is well known for performing histogram-shape-based two-dimensional image thresholding. Otsu's method involves an iteration procedure for all possible threshold values and finding the threshold value at which the sum of solid and void variances multiplied by associated weights has a minimum value. However, the thresholding values extracted using Otsu's method inevitably show large variation when the area of the solid region is changed. Fig. 3 shows a typical variation of thresholding values evaluated from Otsu's method. Since the image set consists of 600 images, the image number 300 represents the cross-sectional image of the center region of the GDL sample. Figs. 3(*a*)–3(*d*) represent the corresponding cross-sectional images obtained by applying Otsu's thresholding method. As shown, the normalized thresholding values are dramatically changed in the positions near the solid surface. Therefore, Otsu's method should be carefully employed in the measurements of porosity distribution in porous media.

Fig. 4 shows a typical vertically sliced image and intensity profile along a horizontal line to explain a new image segmentation method adopted in this study. Every raw image shows small intensity fluctuations owing to X-ray beam fluctuations and other optical aspects. However, the statistically averaged intensity has small variations in the void region marked as a white box in Fig. 4(*b*). Therefore, the image segmentation has to be carefully conducted by comparing the averaged intensity values of the void and solid regions. As shown in Fig. 4(*b*), the intensity of a solid region which corresponds to a fiber has a sharp peak. By selecting a reasonable margin value M in Fig. 4(*b*), the solid area can be segmented quantitatively. The margin value M is obtained by comparing the thickness of a carbon fiber in the segmented image with that in a SEM (scanning electron microscope) image. In this study the value of M is about 5%. Fig. 4(*c*) shows a gray-scale raw image of the sample and its binary image converted using the selected threshold value. We also adopted a median filter that has been commonly used to remove noise embedded in X-ray images (Bjorndal *et al.*, 1999). Since the X-ray μCT system generates inherent noise and arithmetic errors in X-ray images, appropriate filtering and fine segmentation are essential to obtain clear structural information and its accurate measurements.

Fig. 5 represents the variation of thresholding values evaluated from the same image set of Fig. 3. By segmenting using the method described in Fig. 4, the normalized threshold values are almost constant, compared with the large variation of Otsu's method shown in Fig. 3. The small fluctuation in the normalized threshold value is mainly caused by fluctuation of

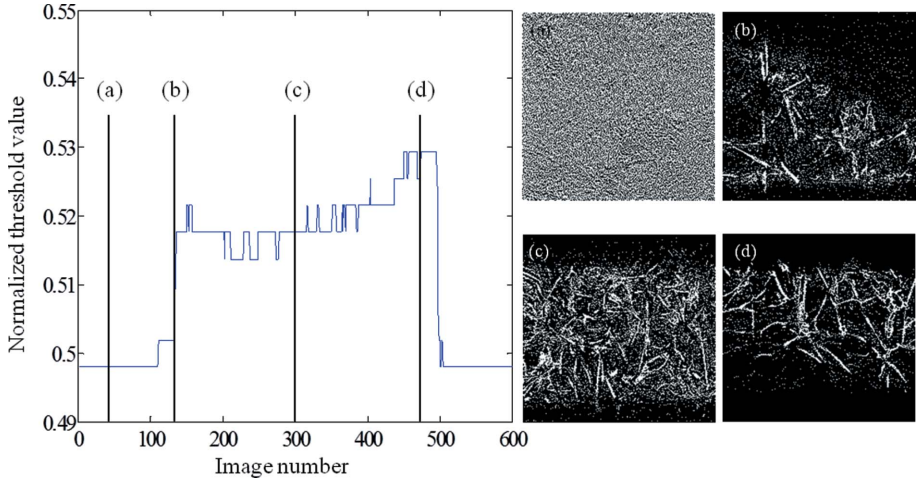

Figure 3
Variation of the threshold value evaluated using Otsu's method.

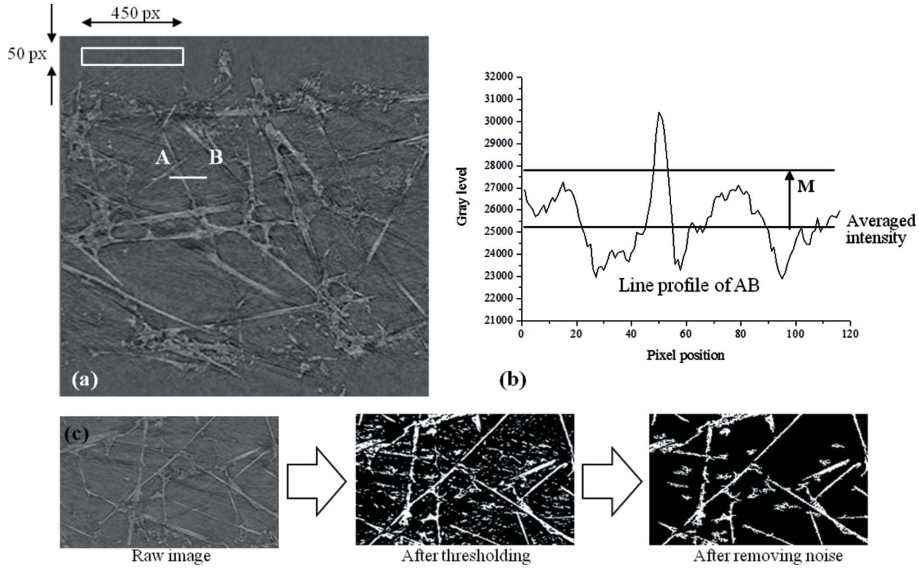

Figure 4
Procedure of image segmentation. (*a*) A typical reconstructed image. (*b*) Intensity variation along the line *AB* in (*a*). (*c*) Digital image processing procedures.

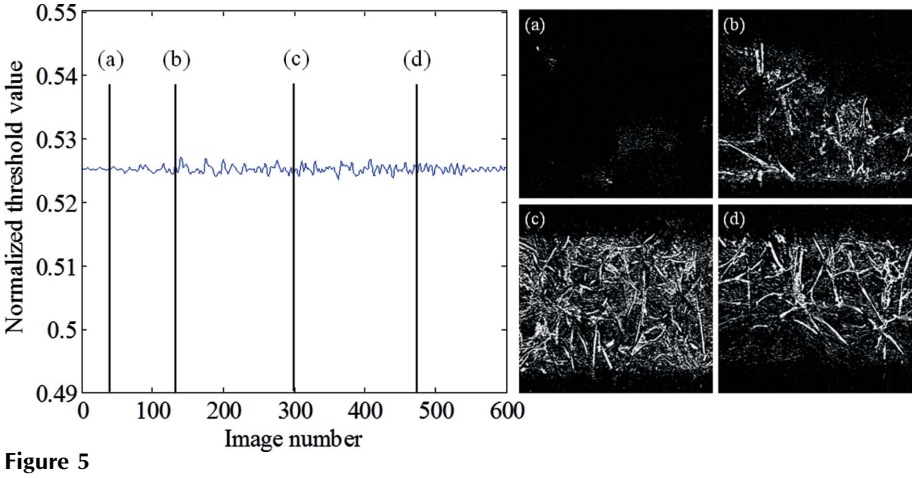

Figure 5
Variation of the threshold value evaluated using the present method.

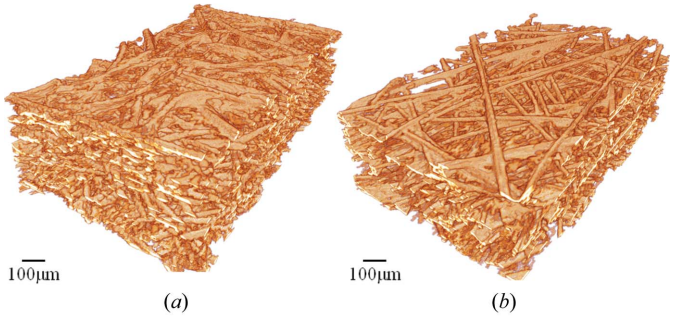

Figure 6
Reconstructed three-dimensional images of (*a*) felt-type and (*b*) paper-type GDLs.

the X-ray beam flux. The adaptive adjustment of the thresholding level of the present method seems to compensate even the small errors due to X-ray beam fluctuations.

Fig. 6 shows three-dimensional tomographic images reconstructed using *AMIRA* software from the segmented binary image of the felt- and paper-type GDLs. The fibers and voids are well segmented and binding materials are also represented clearly. The structural characteristics of two different types of GDLs are clearly shown in the figure such as the fiber diameter, orientation and pore structure. Pores of different size are irregularly located in each sample.

3.2. Porosity distribution under normal state

In general, the porosity of a porous material can be obtained using the following equation,

$$\varepsilon = V_{\text{void}}/V_{\text{total}}. \qquad (1)$$

From equation (1) the porosity value of a single binary image can be calculated by counting the pixels with a value of 0 as the void region and those with a value of 255 as the solid region. As a result, the porosity distribution in the through-plane direction is obtained by enumerating these values.

The X-ray μCT system employed in this study has a spatial resolution of 1 μm, which is not enough to observe the nanoscale porous structures of a microporous layer (MPL). To investigate the temporal and spatial variations of porosity under the freeze-and-thaw cycles, GDL models (35BA and 10BA) without MPL coating were tested.

Fig. 7 compares the porosity distributions of the felt-type and paper-type GDLs in the through-plane direction. The porosity line profile of the felt-type GDL is smoother than that of the paper-type, because the fibers of the felt-type GDL are connected anisotropically. On the other hand, the paper-type GDL has an almost two-dimensional connection. In general, the center region of the GDL has a low porosity value. However, some special regions exhibit lower values than the center region. These abnormal porosity variations result from the morphological defects caused mainly by aggregation of binding materials. Owing to aggregation of supplementary materials, two different phenomena, *i.e.* cavitation and simple aggregation, can be materialized. As shown in Fig. 7, cavitation increases the porosity while the simple aggregation conversely decreases the porosity. Similar morphological defects such as cracks and holes in the GDL

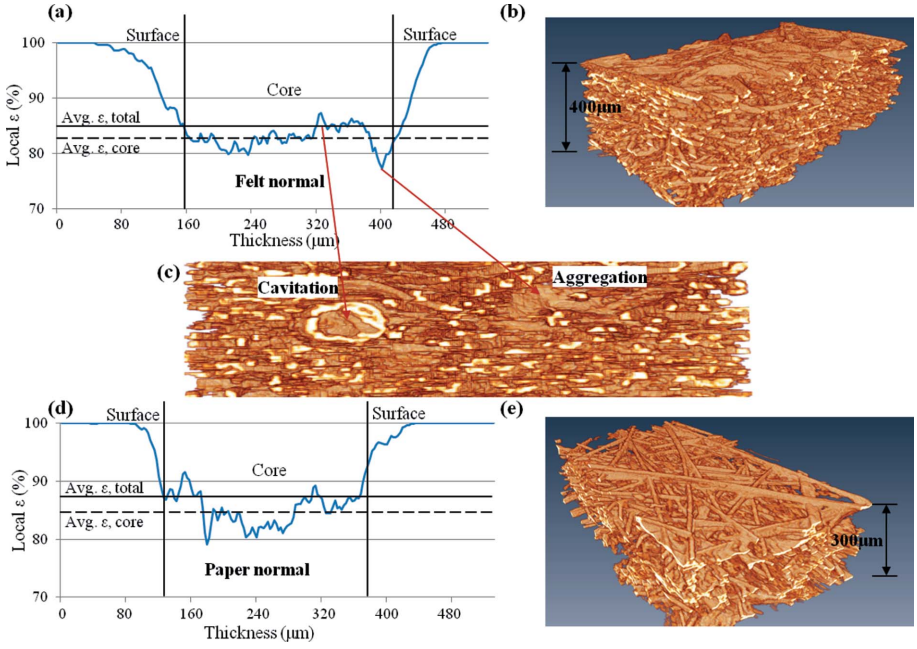

Figure 7
Porosity distribution of the felt- and paper-type GDLs under normal state.

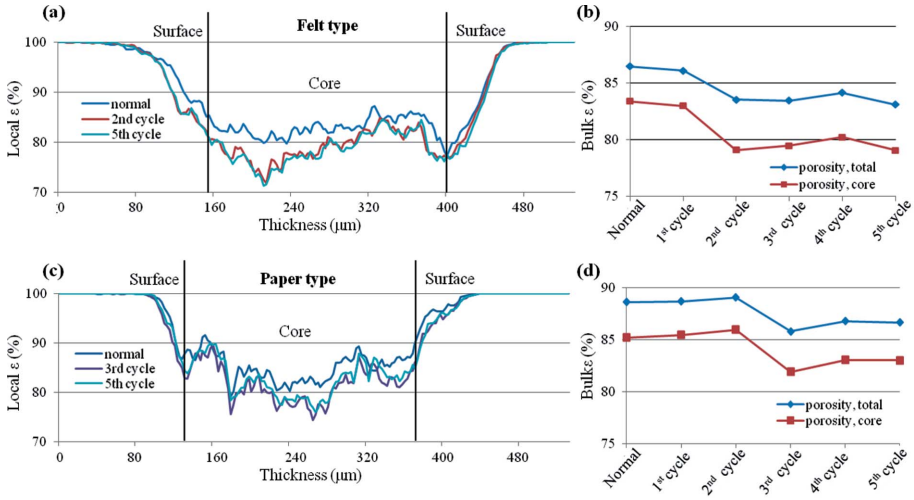

Figure 8
Effects of freeze-and-thaw cycles on the variations of porosity distribution.

attached to a MPL were reported in a previous study (Kim & Lee, 2012). These defects have a strong influence on the porosity distribution and disturb the transport of gas and water in the pore networks of the GDL coincidentally. Polytetrafluoroethylene (PTFE), used for hydrophobic GDL surfaces, is also known to affect the porosity distribution (Fishman & Bazylak, 2011*a*).

Fig. 8 shows the effects of freeze-and-thaw cycles on the variation of the porosity distribution and bulk porosity averaged over the total area of each GDL type. In general, the felt-type GDL has higher porosity values compared with the paper-type GDL owing to the different anisotropic orientation of the fibers. For the felt-type GDL, the porosity is rapidly decreased at the second cycle, while the value drops at the third cycle for the paper-type GDL. The rapid decrease of porosity in the early freeze-and-thaw cycle implies that the inner structure of the GDL experiences irreversible transition. Therefore, it is impossible to recover the original values of the porosities of both GDL samples after a few freeze-and-thaw cycle. In both cases the porosities in the core region show slightly larger variation than the bulk porosities, because the porosities have a smaller variation in the near-surface region than in the core region according to the temperature change. As shown in Fig. 8, all porosity profiles have a similar shape; however, the overall porosities are decreased with the progress of freeze-and-thaw cycles. The structural transformation is basically caused by thermal expansion and shrinkage. Therefore a similar line shape and overall level variation of the porosity distribution line are revealed.

Fig. 9 compares porosity profiles of the paper-type GDL for the freeze-and-thaw state. Every cyclic variation shows almost the same tendency, *i.e.* the porosity decreases in the freezing state and recovers in the thawing state. The decrease of porosity in the freezing state is mostly attributed to shrinkage of the morphological structure and congelation of water vapor inside the GDL. These cyclic porosity-distribution repetitions are directly reflected in the bulk porosity variation as mentioned in our previous study (Kim & Lee, 2012).

Even though the general patterns of the cyclic variations of the porosity distribution are similar, a dissimilar distribution is observed in a specific region. Fig. 10 represents the porosity distribution at the third freeze-and-thaw cycle. As shown in the magnified figure, the line profiles for the freezing and thawing states are somewhat dissimilar. This is mainly attributed to the transformation of the inner morphological structure of the GDL. The relationship between porosity distribution and three-dimensional structural transformation needs to be studied systematically in the near future.

From the porosity distribution, other structural parameters can be estimated using the model proposed by Tomadakis & Sotirchos (1991, 1993). The Tomadakis–Sotirchos (T–S) model was established for randomly oriented fibrous porous media to investigate the infiltration of chemical vapor through fibrous composite materials with porosity gradients. The T–S model is employed to evaluate the heterogeneous tortuosity of the porous GDL using the following equation,

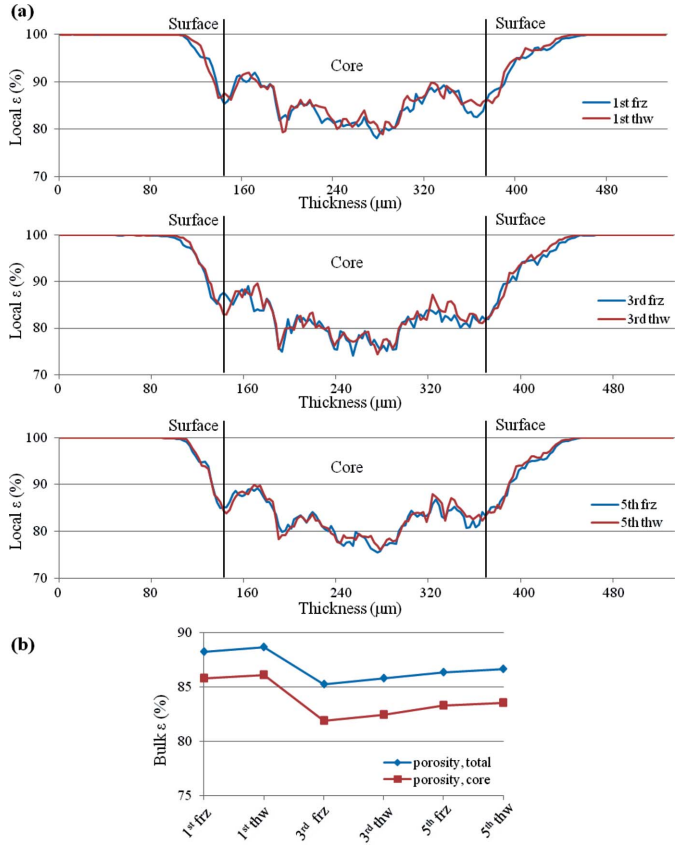

Figure 9
Comparison of porosity variations of the paper-type GDL between the freeze-and-thaw states.

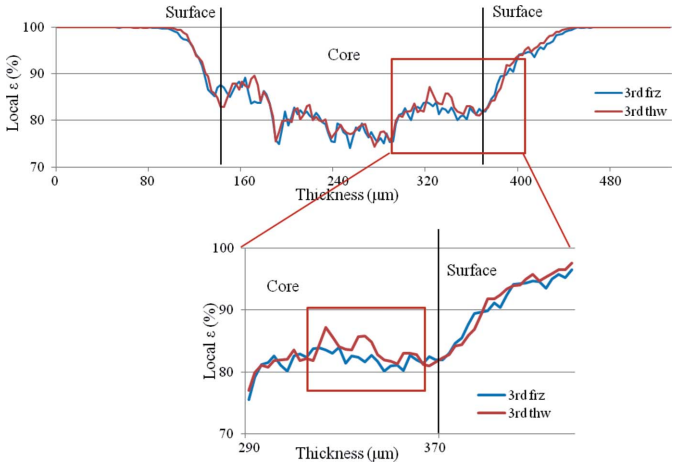

Figure 10
Dissimilar porosity distributions between the freeze-and-thaw states.

$$\tau = \left(\frac{1-\varepsilon_p}{\varepsilon-\varepsilon_p}\right)^{\alpha}, \qquad (2)$$

where the percolation threshold ε_p is 0.11 and the fitted value α is 0.785 for the through-plane direction. These values were founded by Tomadakis & Sotirchos (1991, 1993). This model is also extended to calculate the single-phase permeability in random fibrous and porous media (Tomadakis & Robertson, 2005). The permeability can be calculated using the following equation,

$$K = \frac{\varepsilon}{8(\ln\varepsilon)^2}\frac{\left(\varepsilon-\varepsilon_p\right)^{\alpha+2} r_f^{\,2}}{(1-\varepsilon_p)^{\alpha}\left[(\alpha+1)\varepsilon-\varepsilon_p\right]^2}, \qquad (3)$$

where r_f is the carbon fiber radius. Gostick *et al.* (2006) and Fishman *et al.* (2011*b*) also employed this model and obtained reasonable agreement with experimental results.

Fig. 11(*a*) shows a typical porosity distribution for the felt-type GDL at normal state and the corresponding tortuosity distribution. The distribution of permeability is shown in Fig. 11(*b*). The averaged tortuosity and permeability of the felt-type GDL at normal state are 1.12 and 3.45×10^{-11} m^2, respectively. The tortuosity shows an inversely proportional trend with the porosity, while the permeability shows a similar variation to the porosity profile. The permeability has an almost constant value in the core region of the GDL. However, the permeability rapidly decreases at both ends of the surface regions. The sudden decrease of permeability results in the hindrance of water intrusion during the purging of the PEFC operation.

Fig. 12 shows the variations of the porosity and permeability of the felt-type GDL after the fifth freeze-and-thaw cycle. The porosity is decreased by about 10% at the dashed point, while the permeability is decreased by about 50% at the same point. From these results we can see that a small change of porosity can induce a large variation in the permeability of the GDL.

Since the performance of a PEFC largely depends on the operational conditions of the electrochemical reaction, many parameters can influence the efficiency of the fuel cell. Irreversible variation of the GDL is a typical reason for degradation of the PEFC. Recently, a rapid degradation of output at very early freeze-and-thaw cycles was reported (Lee, Kim, Kim & Li, 2010 *et al.*, 2010; Luo *et al.*, 2010). Therefore, the irreversible porosity variation of the GDL under freeze-and-thaw cycles should be carefully considered in the water management of a PEFC.

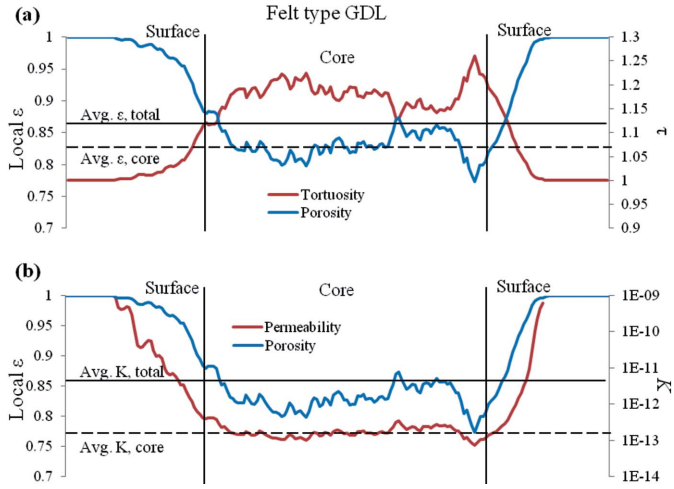

Figure 11
Variations of heterogeneous tortuosity and permeability distribution of the felt-type GDL.

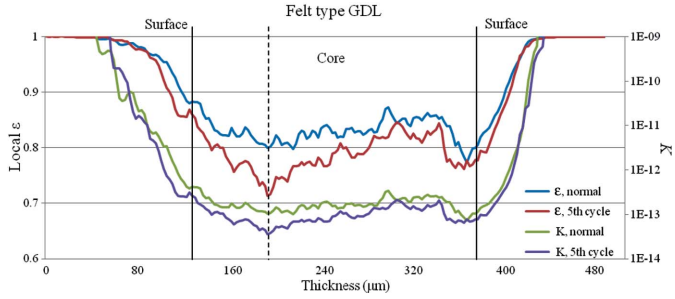

Figure 12
Variation of permeability distribution of the felt-type GDL after fifth freeze-and-thaw cycles.

4. Conclusions

Synchrotron X-ray μCT was employed to visualize the three-dimensional structure of a GDL in a polymer electrolyte fuel cell. Using the adaptive thresholding method, two different types of GDLs are clearly visualized. Moreover, the heterogeneous porosity distributions of GDLs are measured quantitatively. In general, the center region of a GDL generally has the lowest porosity value. The porosity of the GDL was rapidly decreased in the early stage of freeze-and-thaw cycles for both felt- and paper-type GDLs. This rapid decrease of porosity is related to an irreversible structural transformation. The porosity distribution of the GDL shows a cyclic variation according to the repetition of freeze-and-thaw cycles. In a specific region, the porosity distributions at the freezing and thawing states are somewhat dissimilar. This dissimilar

porosity variation is mainly attributed to the structural transformation. The variations of tortuosity and permeability are estimated from the porosity distribution using the T–S model. The heterogeneous permeability distribution shows large variations through freeze-and-thaw cycles, compared with that of the porosity distribution. Conclusively, the repetition and irreversible cyclic variation of the porosity distribution should be considered carefully in the design and water management of a fuel cell system.

The synchrotron X-ray experiments were performed at the 7B2 beamline of the Pohang Accelerator Laboratory (PAL), Pohang, Korea. This work was supported by the Creative Research Initiatives (Diagnosis of Biofluid Flow Phenomena and Biomimetics Research) of MOST/NRF of Korea.

References

Barbir, F. (2005). *PEM Fuel Cells: Theory and Practice*, p. 93. New York: Elsevier Academic Press.

Bjorndal, L., Carlsen, O., Thuesen, G. & Darvann, T. (1999). *Int. Endod. J.* **32**, 3.

Buffiere, J.-Y., Maire, E., Adrien, J., Masse, J.-P. & Boller, E. (2010). *Exp. Mech.* **50**, 289–305.

Cho, E., Ko, J., Ha, H. Y., Hong, S., Lee, K., Lim, T. & Oh, I. (2003). *J. Electrochem. Soc.* **150**, A1667–A1670.

Deville, S., Maire, E., Lasalle, A., Bogner, A., Gauthier, C., Leloup, J. & Guizard, C. (2009). *J. Am. Ceram. Soc.* **92**, 2489–2496.

Fishman, Z. & Bazylak, A. (2011*a*). *J. Electrochem. Soc.* **158**, B841–B845.

Fishman, Z. & Bazylak, A. (2011*b*). *J. Electrochem. Soc.* **158**, B247–B252.

Fishman, Z., Hinebaugh, J. & Bazylak, A. (2010). *J. Electrochem. Soc.* **157**, B1643–1650.

Gallagher, K. G., Darling, R. M., Patterson, T. W. & Perry, M. L. (2008). *J. Electrochem. Soc.* **155**, B1225–B1231.

Gostick, J. T., Fowler, M. W., Pritzker, M. D., Ioannidis, M. A. & Behra, L. M. (2006). *J. Power Sources*, **162**, 228–238.

Kim, S. & Lee, S. (2012). *Int. J Hydrog. Energy*, **37**, 566–574.

Lee, S., Kim, S., Park, G. & Kim, C. (2010). *Int. J. Hydrog. Energy*. **35**, 10457–10463.

Lee, Y. T., Kim, B. S., Kim, Y. C. & Li, X. (2010). *J. Power Sources*, **196**, 1940–1947.

Li, J., Lee, S. & Roberts, J. (2008). *Electrochim. Acta*, **53**, 5391–5396.

Luo, M., Huang, C., Liu, W., Luo, Z. & Pan, M. (2010). *Int. J. Hydrog. Energy*. **35**, 2986–2993.

Otsu, N. (1979). *IEEE Trans. Syst. Man Cybern.* **9**, 62–66.

Park, G., Lim, S., Park, J., Yim, S., Park, S., Yang, T., Yoon, Y. & Kim, C. (2010). *Curr. Appl. Phys.* **10**, S62–S65.

Radon, J. H. (1917). *Ber. Verh. Sächs. Akad. Wiss. (Leipzig)*, **69**, 262–277.

Stock, S. R. (2008). *Int. Mater. Rev.* **53**, 129–181.

Tomadakis, M. M. & Robertson, T. (2005). *J. Compos. Mater.* **39**, 163–188.

Tomadakis, M. M. & Sotirchos, S. V. (1991). *AlChE J.* **37**, 74–86.

Tomadakis, M. M. & Sotirchos, S. V. (1993). *AlChE J.* **39**, 397–412.